

Comprehensive Mapping of the Island Arc Rocks in the Marahiq Area, South Eastern Desert, Egypt

Ashraf Emam^{*1}, Nedal Qaoud², Ezzat Abdel-Rahman¹ and Khairiya M. Fawzy¹

¹Geology Department, Faculty of Science, Aswan University, Egypt

²Geology Department, Faculty of Science, Al-Azhar University, Gaza, Palestine

Abstract: Remote sensing and geochemical data are used to discriminate between the different varieties of island arc assemblage covering Marahiq area, South Eastern Desert of Egypt. The Precambrian basement rocks exposed in the study area comprise ophiolite and island arc assemblages. The ophiolitic rocks include serpentinites and talc-carbonate, while the metavolcanics and metavolcanosedimentary rocks represent the island arc assemblage. Petrographically, the island arc units are differentiated into metabasalt, meta-andesite, metadacite, meta-andesitic tuffs, chlorite talc schist and biotite chlorite schist. The geochemical data revealed that these metavolcanics and metavolcanosedimentary rocks are calc-alkaline to tholeiite in nature with low to medium-K, and likely represent an immature island arc. Image processing techniques applicable to the Enhanced Thematic Mapper (ETM+) data are used for mapping and delineating exposures of the different island arc units at the Marahiq area. Principal component analysis, minimum noise fraction and band rationing techniques provide efficient data for lithological mapping. New detailed map was generated as a result of the processed ETM+ images.

Keywords: Remote sensing, island arc, band ratios, geochemistry, Marahiq, Egypt.

1. INTRODUCTION

The Marahiq area is part of the Arabian-Nubian Shield (ANS), about 90 km², in the South Eastern Desert of Egypt between latitudes 22° 28' and 22° 33'N, and longitudes 33° 26' and 33° 31'E, (Fig. 1). The Precambrian basement rocks of the ANS in the Eastern Desert are viewed mostly as an orogenic amalgamation of island arcs, immature basin sediments and oceanic crust. These different terrains were developed during the Pan-African cycle (between 900 and 600 Ma) in an oceanic environment [1] or probably in a back arc basin [2] offshore of the East Sahara Craton. According to the close association of ophiolite assemblage and the calc-alkaline island arc volcanics, several models have been proposed for the structure and evolution of the Pan-African belt in the ANS [3-14]. The crustal evolution of the ANS started some 950 Ma ago and was summarized through four main stages [15]. During the first and second stages (950-850 Ma and 850-650 Ma, respectively) the rifting of the supercontinent "Rodinia" was followed by sea-floor spreading and the initiation of subduction resulted in formation of oceanic crust and island arcs terrains. The end of second stage was dominated by welding and accretion of oceanic and island arc terrains to form the ANS. The third stage (650-580 Ma) is the post-collision batholithic stage, characterized by large-scale calc-alkaline magmatism, mainly of intermediate to felsic composition.

The fourth stage (600-530 Ma), so-called the post-orogenic stage, involves igneous activity of mainly alkaline to peralkaline granites, andesites, rhyolites, and several episodes of dike swarms representing intra-cratonic within-plate magmatism. The common association of island arc metavolcanics and the plutonic rocks (gabbros, diorites, tonalites and/or granodiorites) in both space and time favors that they are co-magmatic [8, 16]. El-Kazzaz [17] summarized three principal tectonic stages for the development of rocks occupying the central Wadi Allaqi: a) an early rock-forming volcano-sedimentological stage which has involved some extension. b) an accretion stage involving contraction, the formation of thrust-duplexes, and orogenies which may be related to collision of east and west Gondwana. c) a collapse of the tectonic pile. Initially, an island-arc with an extensional back-arc basin towards the Nile Craton and a subduction-zone in the opposite direction was formed. El Kazzaz and Taylor [18] established three main tectonic-stratigraphic successions, covering the area of central Wadi Allaqi. The most appropriate tectonic environment for the deposition of these successions, based upon petrological considerations, is a back-arc basin. The present work deals with the geologic setting, petrography, spectral characteristics and geochemistry of the outcropping island arc rocks of the Marahiq area. The comprehensive mapping and geochemical characterization of the island arc rocks are the main objectives of the current study.

2. METHODOLOGY

For lithologic mapping and discrimination between the different island arc units, subsets of Enhanced Thematic

*Address correspondence to this author at the Geology Department, Faculty of Science, Aswan University, Egypt; Tel: +20 97 3480450; Fax: +20 97 3481533; E-mail: ashrafemam99@hotmail.com

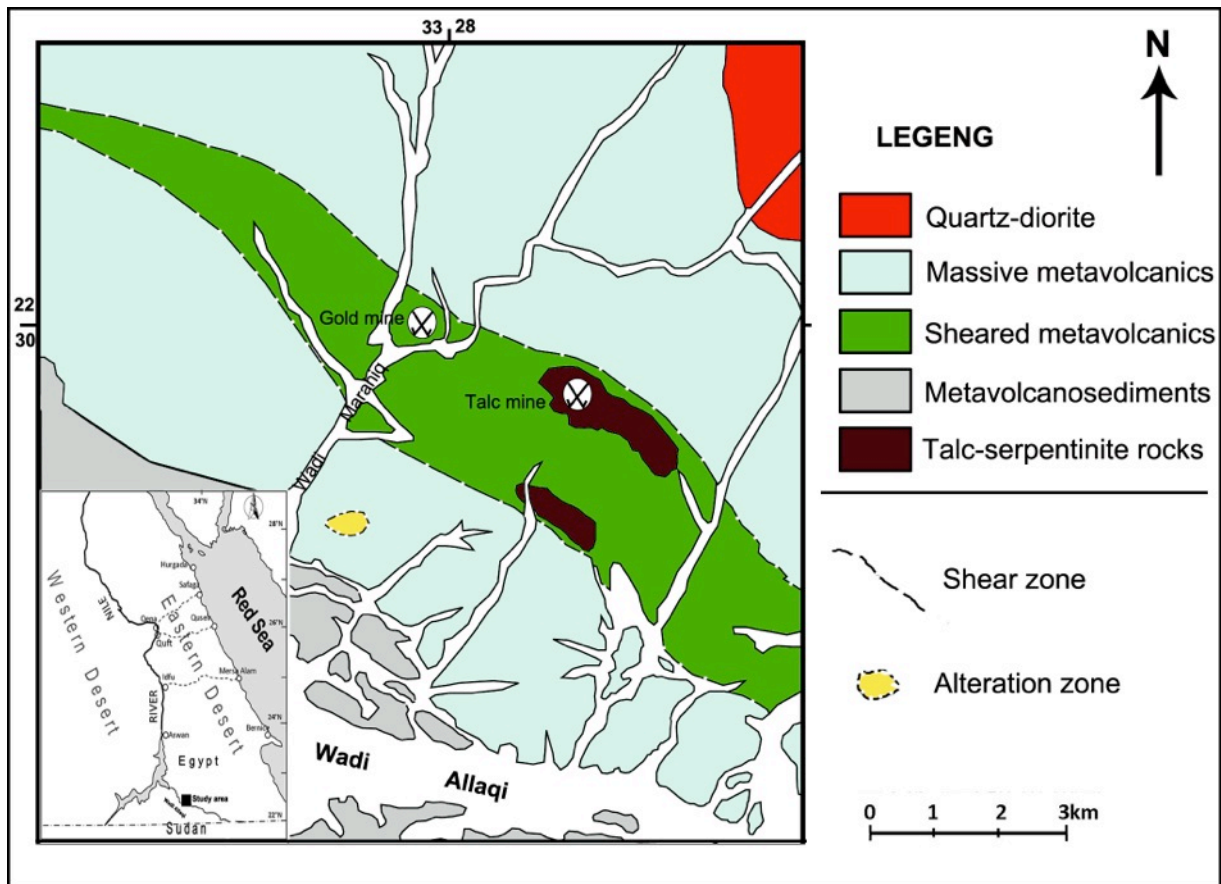


Fig. (1). Geologic map of Marahiq area, SE Desert of Egypt, modified from Emam [19].

Mapper (ETM+) data (174/44 path/row, acquisition date 09/03/2005) have been processed using the ENVI 4.5 (ENVI® image processing and analysis software, from ITT Visual Information Solutions). The present study includes the use of band rationing and principal component transformation techniques to facilitate mapping the island arc units. During field work, a total of 75 rock samples were collected from ophiolitic serpentinites and island arc assemblages and 40 thin sections were prepared for microscopic investigation. Seventeen representative samples of island arc metavolcanics, metapyroclastics and biotite-chlorite schists were chemically analyzed for major oxides and trace elements. The chemical analyses were carried out by means of X-ray Fluorescence Spectrometer (XRF) at the laboratories of Nuclear Materials Authority, Egypt.

3. GEOLOGIC SETTING

The Neoproterozoic rocks covering the Wadi Allaqi region include mafic-ultramafic ophiolitic assemblage, at least two volcanosedimentary-plutonic island-arc assemblages and late- to post-tectonic granitic intrusions [2, 7, 15, 20-22]. According to El-Kazzaz [17], the central Wadi Allaqi is composed mainly of Neoproterozoic volcanic, sedimentary and volcanosedimentary rocks, which were deformed and metamorphosed to green-schist facies during the Pan-African orogeny, probably lasting from 750 Ma to 650 Ma. In Marahiq area, a part of Wadi Allaqi region, the exposed units are ophiolitic and island arc rocks, intruded by

quartz-diorites and invaded by basic to acidic dykes as well as quartz veins.

Ophiolite assemblage comprises serpentinites and their related talc-carbonate rocks that represent the oldest rock units in the study area. They form small, curved and stretched lensoidal bodies and huge elongated masses along NW-trending shear zone in the eastern part of mapped area. They tectonically interlace the sheared metavolcanics and metavolcano-sedimentary rocks, exhibiting sharp structural contact. Most of the serpentinite masses are highly sheared and altered to talc and talc-carbonates with relics of serpentinite (Fig. 2A). The resultant talc-carbonates have yellowish brown to light cream colors and cavernous shapes. Basic to intermediate dykes and quartz veins are cutting through these talc-carbonates in the eastern side of the Marahiq area. *Island arc assemblage* comprises varieties of metavolcanics and metavolcanosedimentary rocks. The metavolcanics cover large parts of the mapped area, specially at the northern and western sides. They form moderate to high hills and elongated rock masses (Fig. 2B), exhibiting fine to medium-grained textures. Along shear zones, they are highly sheared and exhibit NW foliations. These metavolcanics comprise metabasalt, meta-andesite, metadacites and their equivalent metapyroclastics (meta-agglomerates and meta-tuffs). The meta-basalt and meta-andesite are amygdaloidal and porphyritic. The metavolcanics are cut by many basic, intermediate and acidic dykes and gold sulfide-bearing quartz veins. The metavolcano-sedimentary rocks display well schistosity and

are represented principally by chlorite-talc schist and biotite-chlorite schist. These island-arc rocks are dominantly lying in the southern part of the Marahiq area. They exhibit greenish gray to dark gray colors, and forming low to moderate hills and elongated masses. They exhibit a well foliation, striking NW-SE and dipping 64° in the NE direction in the southern side of the studied area (Fig. 2C). Along the shear zones in the eastern side of the mapped area, they are intensively fractured and foliated. These rocks are jointed and traversed by two sets of joints forming a pencil shape structure. *Quartz-diorites* are found in the northeastern corner and extend beyond the limit of the mapped area. They are represented by massive bodies that have grey green color with milky phenocrysts of plagioclase. Quartz diorites exhibit medium to coarse-grained, subhedral granular texture, while their marginal parts show porphyritic texture. The contact between quartz diorites and metavolcanics is sharp. *Dykes and quartz veins* cut through the different rock units occurring in the studied area. They extend NW-SE parallel to fault planes and shear zones cutting across the studied area. These dykes are mainly basic to intermediate in composition (Fig. 2D), where the acidic dykes have a limited distribution. They have thickness (1-2.5m) and length up to several hundreds of meters. The quartz veins are mainly milky and concentrate in the central part of the area along the NW-trending shear zones. They cut through the

metavolcanics and have a thickness ranging from 40 cm to 2 m and length of 10-200m.

4. PETROGRAPHY

4.1. *Serpentinites* are characterized by mesh texture. They are composed mainly of antigorite and lizardite, associated with variable amounts of talc, chlorite and carbonate minerals (Fig. 3A). Chromite and magnetite occur as accessory minerals. Antigorite occurs as colorless to pale green, fibrous aggregates and tiny flakes with low relief. Lizardite occurs as very fine streaks and fibers which dissected in two perpendicular directions, leaving in between rectangular areas, filled with talc.

4.2. *Meta-basalts* include ophitic meta-basalt and amygdaloidal meta-basalt. They comprise plagioclase, pyroxene and tremolite-actinolite as essential mineral constituents. In the *ophitic metabasalt*, plagioclase occurs as colorless, subhedral, tabular and lath-like crystals that partially altered to sericite, epidote, saussurite and calcite. Most plagioclase crystals are enclosed partly and/or totally within pyroxene to form ophitic and subophitic textures (Fig. 3B). Pyroxene is represented mainly by short prismatic and lath-like crystals of augite. These crystals are colorless to pale green in color, cut by plagioclase crystals and partially

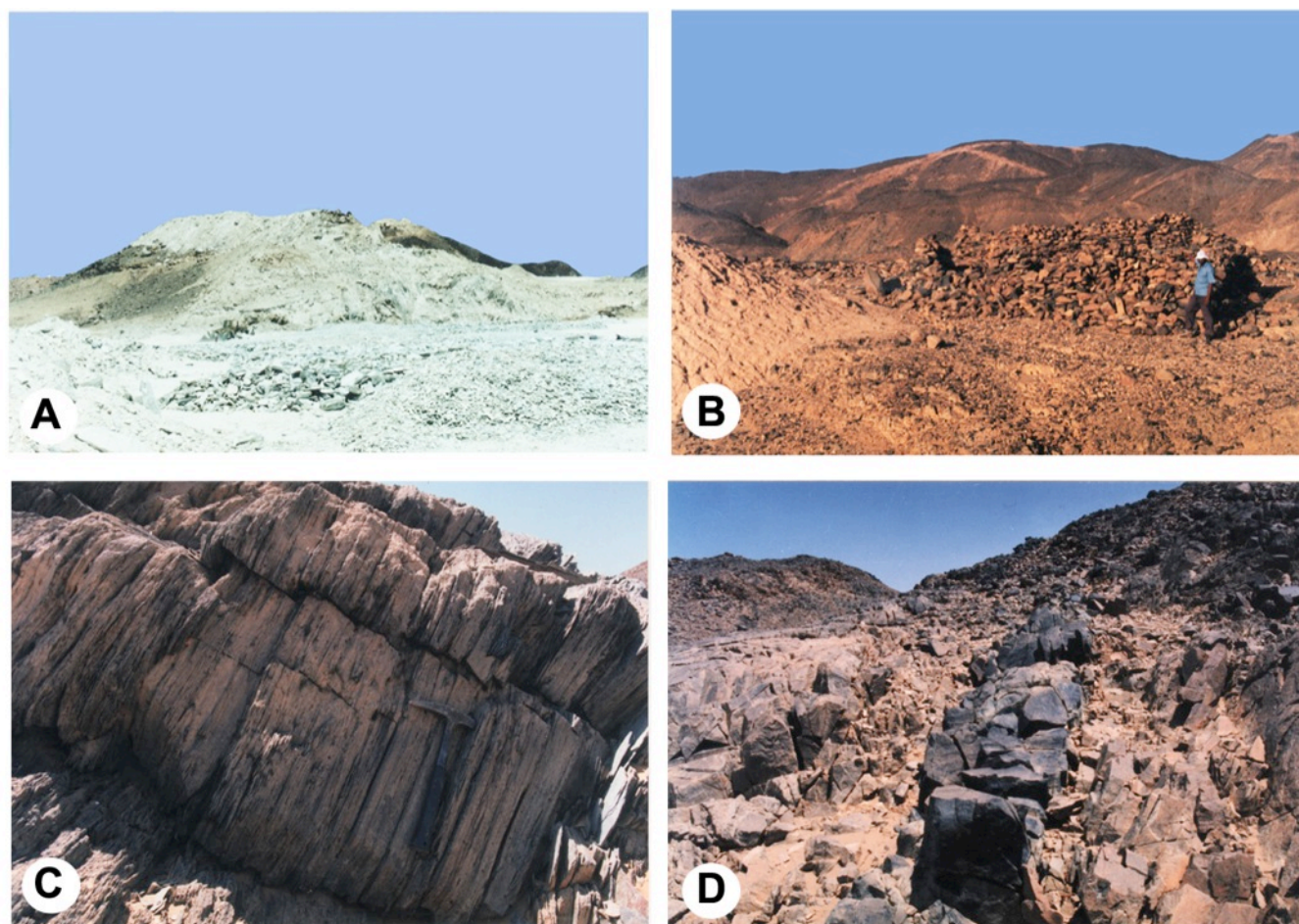


Fig. (2). A) Serpentinite exposures and talc and talc-carbonate rocks within the shear zones. B) Elongate hills of metavolcanics are invaded with gold-sulfide bearing quartz veins. C) Close up view showing well foliated metavolcanosedimentary rocks. D) Basic dyke (1 m thick) extends NW-SE and cut across the sheared metavolcanics.

altered to chlorite and calcite. Tremolite-actinolite occurs as colorless to olive green, elongated needles and columnar crystals that altered to chlorite and calcite, and some crystals enclose inclusions of pyroxene and opaques. Epidote occurs as fine aggregates and irregular patches, throughout the groundmass, replacing plagioclase. Chlorite occurs as minute, fibrous and acicular crystals as well as irregular patches scattered throughout the groundmass. Sericite occurs as colorless, minute fibrous crystals and flakes, replacing

plagioclase. Subhedral to anhedral crystals of calcite are scattered within the matrix and filling the microveinlets. Fine disseminated grains of iron oxides are scattered within the matrix and along the microveinlets.

In the *amygdaloidal meta-basalt*, plagioclase occurs as fine tabular crystals, randomly distributed throughout the groundmass. Pyroxene occurs as fine-grained, anhedral to subhedral crystals and aggregates of augite, while tremolite-

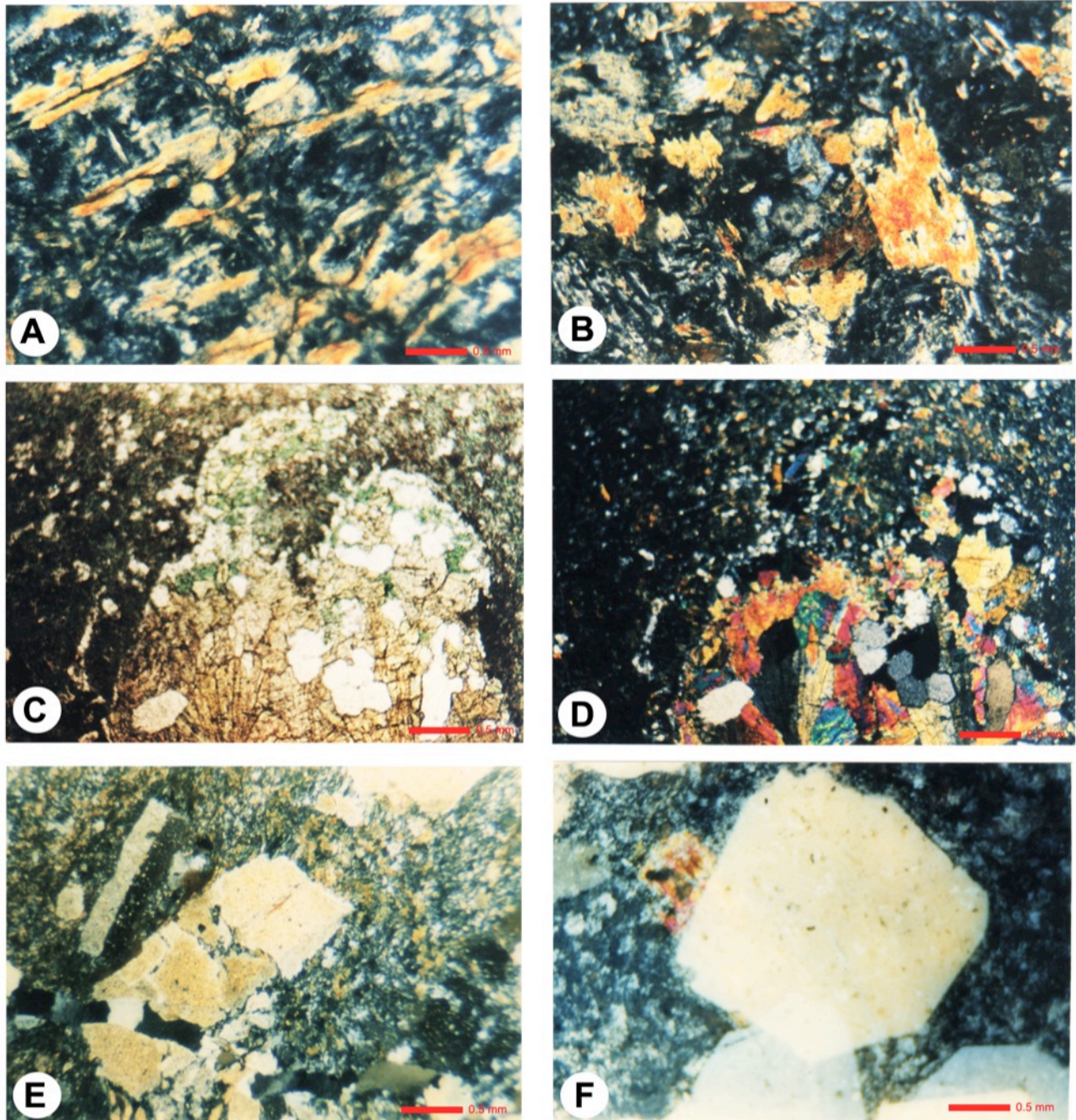


Fig. (3). A) Fibrous and acicular antigorite crystals highly altered to talc in the serpentinite rocks. B) Plagioclase crystals partly and totally invade pyroxene laths in ophitic meta-basalt. C) PPL view of amygdaloidal meta-basalt shows amygdales filled with epidote (yellowish), chlorite (greenish) and quartz (color-less). D) CN view of amygdaloidal meta-basalt shows epidote with high interference colors and six-sided quartz crystals within amygdales. E) Quartz microveinlet cutting across highly altered and microfaulted plagioclase phenocrysts in porphyritic meta-andesite. F) Porphyritic texture in meta-dacite porphyry, where large euhedral quartz phenocrysts set in a fine-grained matrix.

actinolite occurs as colorless to olive green fibrous aggregates, distributed within the groundmass and altered to chlorite. Epidote occurs as euhedral to subhedral, prismatic crystals filling the amygdals and associated with quartz and chlorite (Fig. 3C, D). It also occurs in the matrix around the amygdals as anhedral fine crystals and patchy aggregates, replacing plagioclase.

4.3. *Meta-andesites* are characterized by porphyritic texture and composed essentially of plagioclase, pyroxene, actinolite and hornblende phenocrysts and microphenocrysts, embedded in a fine-grained groundmass, composed of the same mineral constituents with little amounts of quartz, biotite and iron oxides, as accessories. Sericite, epidote, chlorite and calcite are secondary minerals. Plagioclase is represented by colorless subhedral, tabular, prismatic and lath-like phenocrysts (Fig. 3E). They show corroded outlines, internal cracks and occasionally microfaults due to deformation. Pyroxene occurs as subhedral, short prismatic and lath-like crystals of augite with pale green color. They also are slightly altered to actinolite and chlorite. Actinolite occurs as long prismatic, tabular and columnar subhedral crystals with frayed edges and pale green color. Hornblende is represented by subhedral, prismatic, highly corroded and cracked crystals, with high relief and greenish brown color. They are corroded and slightly to highly altered to actinolite, chlorite and calcite. Fine-grained, subhedral laths and flakes of biotite is scarce and commonly altered to chlorite.

4.4. *Meta-dacite porphyries* are composed mainly of porphyritic phenocrysts of quartz, plagioclase and biotite, encountered in a fine-grained groundmass with the same mineral constituents and variable amounts of chlorite, sericite, epidote and calcite as secondary minerals, while the iron oxides are the main accessories (Fig. 3F). Plagioclase forms colorless, euhedral to subhedral, tabular, prismatic and lath-like phenocrysts. They are moderately to highly altered to sericite, epidote and calcite. Quartz forms well crystallized, colorless, euhedral, porphyritic phenocrysts which are cracked and corroded by the groundmass. Biotite occurs as subhedral, lath-like phenocrysts and large flakes with brown color and moderate pleochroism, from brown to

yellowish colors. It is commonly altered to chlorite and highly corroded by the constituents of the matrix.

4.5. *Meta-pyroclastics* are distinguished to two varieties; andesitic lithic crystal meta-tuffs and laminated meta-tuffs. The andesitic lithic crystal meta-tuffs are composed essentially of lithic fragments, plagioclase and quartz crystal fragments, embedded in tuffaceous groundmass, commonly composed of microcrystals and fine ashes of quartz, plagioclase, actinolite, epidote, chlorite, calcite and iron oxides (Fig. 4A). The laminated meta-tuffs are composed of fine-grained tuffaceous laminae alternate with very fine-grained tuffaceous ones. These tuffaceous laminae possess the same mineral constituents as plagioclase, quartz and calcite. The fine laminae contain chloritized hornblende and actinolite, whereas the more finer laminae are rich in iron oxides and graphite.

4.6. *Chlorite-talc schists* are characterized by greenish white color and composed essentially of quartz, plagioclase, talc and chlorite (Fig. 4B). Quartz occurs as colorless, anhedral to subhedral, elongated crystals and as fine-grained aggregates, which are stretched parallel to the schistosity and alternating with the fine-grained matrix. Plagioclase occurs as subhedral, tabular, small crystals and fine laths, oriented with their longer dimensions parallel to the schistosity of the rock. These crystals are highly broken and altered to sericite. Talc is abundant in these rocks, occurring as fine-grained, anhedral crystals and flakes, scattered throughout the groundmass and aligned parallel to the schistosity. It is commonly associated with calcite and the individual flakes show simple twinning. Chlorite occurs as pale green, anhedral flakes, associated with talc.

4.7. *Biotite-chlorite schists* consist essentially of quartz, plagioclase, chlorite and biotite, while the iron oxides are accessories. Quartz occurs as fine-grained, allotriomorphic crystals and aggregates. They possess suture outlines and most of them are stretched parallel to the planes of schistosity. Plagioclase occurs as anhedral to subhedral lath-like crystals which are highly corroded by quartz and altered to sericite. Biotite occurs as small subhedral, flakes and strings with brown color. Chlorite forms small, anhedral,

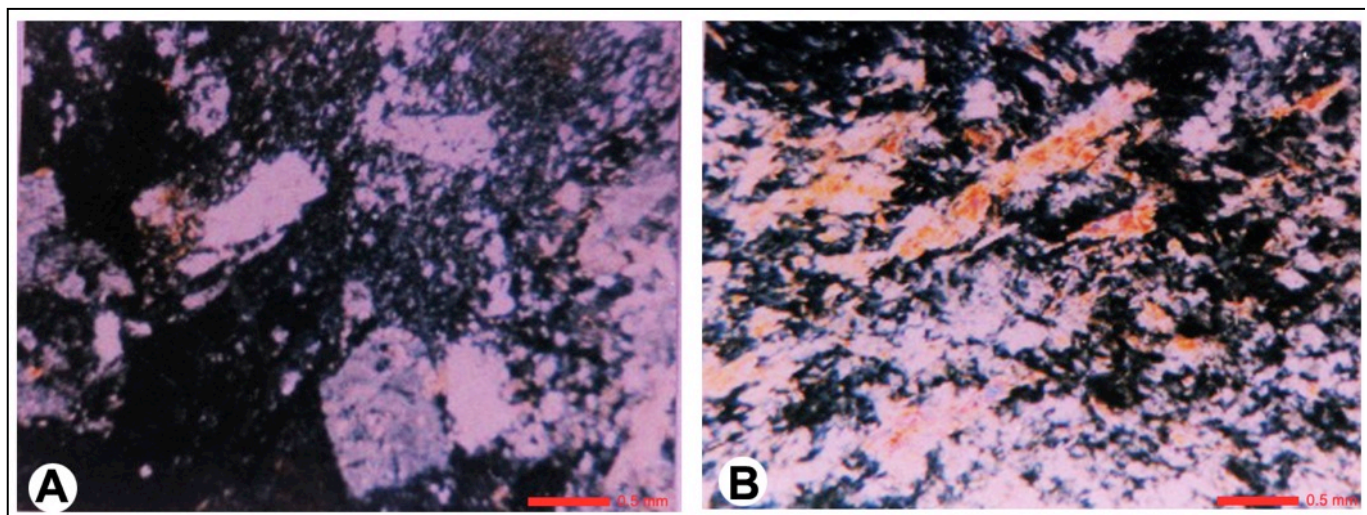


Fig. (4). A) Andesitic lithic fragments, quartz and altered plagioclase set in tuffaceous matrix of lithic crystal meta-tuffs. B) Talc (yellowish) and chlorite (dark) flakes are arranged parallel to schistosity of chlorite-talc schists.

fibers and flakes, distributed subparallel to the planes of schistosity.

5. GEOCHEMISTRY

5.1. Petrochemical classification and nomenclature. Seventeen representative samples of island arc metavolcanics, metapyroclastics and biotite-chlorite schists were chemically analyzed for major oxides and trace elements (Table 1). The analyzed samples are plotted on the $\text{Na}_2\text{O}+\text{K}_2\text{O}$ versus SiO_2 (TAS) diagram [23]. The metavolcanics and their metatuffs occupy basalt, basaltic andesite, andesite and dacite fields, while the metavolcanosediments spread over dacite and rhyolite fields (Fig. 5A). One metabasalt sample lies on the boundary between the basalt and basaltic andesite fields, whereas two meta-andesitic tuff samples occur near the boundary between andesite and dacite fields. This may be attributed to that such samples are affected by silicification process within the shear zone (SH-I). On the K_2O versus SiO_2 diagram [23], the studied metavolcanics, metatuffs and metavolcanosediments lie within the low-K and medium-K fields, except an andesite sample which lies in the high-K field (Fig. 5B). We can conclude that the metavolcanic samples range in composition from basalt, andesite to dacite, while the metavolcano-sedimentary samples occupy the dacite and rhyolite field.

5.2. Magma type. Plotting the chemical data of the investigated rocks on the $\text{Na}_2\text{O}+\text{K}_2\text{O}$ versus SiO_2 diagram [24] illustrates that all the samples fall in the subalkaline field (Fig. 5C). On the AFM diagram [24] the basalt and meta-andesitic tuff samples lie in the tholeiitic field, whereas the meta-andesite samples occupy the calc-alkaline field (Fig. 5D). One metadacite sample lies within the tholeiitic field while the other two samples plot along the boundary between tholeiitic and calc-alkaline fields. The metavolcanosediments plot within both tholeiitic and calc-alkaline fields. The plots of metadacite, meta-andesitic tuffs and metavolcanosediments in the tholeiitic field are due to the ferrugination process within shear zones and consequently an increase in FeO total.

On the $\text{Al}-(\text{Fe}^{\text{total}}+\text{Ti})-\text{Mg}$ diagram [25], the analyzed samples of metabasalt fall within the tholeiitic basalt field. On the other hand, the samples of meta-andesite, meta-andesitic tuffs, metadacite and schists plot in the calc-alkaline field, except one sample from metadacite and another from schists lie in the tholeiitic basalt field (Fig. 6A). The plotting of the analyzed samples on the Log Cr versus silica diagram [26] demonstrates that all plots of metabasalt fall in the tholeiitic field, while those of meta-andesite, meta-andesitic tuffs, metadacite and schists fall in the calc-alkaline field, except one sample (Fig. 6B). Moreover, all plots of the analyzed samples fall in the low-potassium tholeiites field of the Log Cr-Log Ti diagram [27] except three metabasalt samples lying in the ocean floor basalts field due to their enrichment of chromium and titanium (Fig. 6C).

5.3. Tectonic setting. The TiO_2 versus FeO^*/MgO binary relationship of Miyashiro [28] reveals that the analyzed samples plot within and close to the island arc field (Fig. 6D). The relationship between Log Cr and FeO^*/MgO [26]

shows that the analyzed samples fall mostly within the field of island arcs and active continental margins (Fig. 7A). The Log Ni versus FeO^*/MgO diagram [29] discriminates the island arc tectonic setting for these rocks (Fig. 7B). By plotting the samples of metavolcanic and metavolcanosedimentary rocks onto the potash-silica diagram [30], it appears that these samples plot within the tholeiitic field of Central Kuriles and spread over the calc-alkaline field of Cascades, (Fig. 7C).

6. REMOTE SENSING DATA ANALYSIS

6.1. Principal component analysis (PCA). The principal component analysis is the image processing technique commonly used for analysis of correlated multidimensional data. It is multivariate statistical method used to compress multispectral data sets by calculating a new coordinate system and redistribute data onto a new set of axes in multidimensional space [31-33]. The PCA may be carried out for multispectral data sets consisting of any number of bands to produce sets of perpendicular PC-axes; each PC-axis has new pixel values [34]. The obtained PC-images may be displayed separately as single stretched PC-images or used as a component in color composite PC-image. According to Singh and Harrison [35], two types of principal component analysis can be distinguished, depending on the procedure by which the principal components are mathematically calculated. The un-standardized PCA uses the covariance matrix obtained from the input multispectral data, whereas the standardized PCA uses the correlation coefficients instead of covariance matrices for calculating the principal components. The principal component transformation has several advantages, where most of the variance in a multispectral data set is compressed into one or two PC-images. Moreover, noise may be relegated to the less correlated PC-images and the spectral differences between materials may be more apparent in PC-images than in individual bands [36].

The PCA was applied on the six ETM+ bands covering VNIR and SWIR regions. The eigen values as well as variances% for each band were calculated and shown in (Table 2). Furthermore, PC-images and false color composite PC-images were generated. The PC1 includes 93.50% of the information content of the image whereas PC2, PC3 and PC4 mark 5.16%, 0.67% and 0.37% respectively. The fourth principal component image (Fig. 8A) delineates the altered rocks along shear zone, which show white image signature.

The false color composite PC-image (Fig. 8B) processed from PC1 in Red, PC2 in Green and PC4 in Blue, identifies the alteration zones and distinguishes between metavolcanosediments and metavolcanics cropping out through Marahiq area. The alteration zones show rose, yellowish and light-blue image signatures, whereas the metavolcanosediments exhibit lemon and bluish green image signatures. The meta-andesites and metabasalts show dark blue and dark green image signatures, respectively. On the other hand, this FCC PC-image failed to differentiate between the metadacite and quartz diorite that show the same greenish image signature.

Table 1. Chemical Analyzes and Calculated CIPW Norms of Marahiq Island arc Assemblage

Sample	Metabasalts				Meta-Andesites				Metadacites			Meta-Tuffs			Biotite-Chlorite Schists		
	1	2	3	4	5	6	7	8	9	10	11	12	13	14	15	16	17
Major Oxides (wt%)																	
SiO ₂	49.43	50.48	51.84	50.2	60.78	61.71	59.74	55.4	66.65	68.72	66.25	63.36	61.4	62.7	71.86	74.68	70.6
TiO ₂	1.25	1.05	0.89	0.4	0.51	0.41	0.46	0.8	0.33	0.41	0.2	0.1	0.2	0.2	0.11	0.05	0.4
Al ₂ O ₃	12.34	11.94	11.51	13.9	12.1	12.08	11.5	13.9	11.43	10.91	13.79	12.29	15.1	14.9	9.68	10.59	14.8
Fe ₂ O ₃	16	15.8	15.2	10.9	9.8	7.86	3.2	8.3	7.2	8	6.2	8.8	9.3	8.7	7.2	2.8	3.2
MnO	0.23	0.19	0.15	0.2	0.14	0.1	0.06	0.1	0.11	0.16	0.1	0.07	0.1	0.1	0.08	0.02	0.01
MgO	4.1	5.4	6.6	9.9	3.3	4.6	4.4	7.7	2.4	1.6	2.1	2.4	2.9	1.5	0.8	1.4	2.1
CaO	8.4	7.96	7.72	8.8	2.8	3.24	11.2	6.5	7.64	4.48	5.3	8.32	5.7	5.2	1.12	3.4	4.3
Na ₂ O	2.36	2.18	2.09	2.5	4.99	2.9	1.22	2.5	1.48	2.85	2.3	1.22	1.9	2.1	4.66	3.64	2.4
K ₂ O	0.84	0.56	0.37	0.5	1.39	2.02	3.35	1.2	1.58	1.17	1.6	1.95	1.3	1	0.7	0.95	1.4
P ₂ O ₅	0.92	0.83	0.81	0.1	0.97	0.39	0.85	0.1	0.54	0.43	0.1	0.93	0.2	0.05	0.1	0.29	0.1
LOI	2.51	2.45	2.37	1.7	1.56	3.22	2.84	2.5	0.6	1.23	1.4	0.55	1.6	1.6	3.66	1.61	0.4
Total	98.38	98.84	99.55	99.1	98.34	98.53	97.82	99	99.96	99.96	99.34	99.99	99.7	98.05	99.97	99.43	99.71
Trace Elements (ppm)																	
Sr	1079	892	426	372	265	385	331	267	108	132	72	158	169	162	160	131	105
Rb	11	18	23	12	35	42	37	52	98	125	132	21	28	24	12	10	17
Y	31	58	134	62	137	36	86	78	293	169	215	118	112	123	211	90	190
Ba	195	132	157	162	463	568	447	481	1205	1126	1182	297	203	189	115	103	79
Cr	63	64	67	47	16	18	15	11	13	14	12	12	11	16	6	9	11
Co	43	37	54	46	34	33	31	37	12	10	11	23	31	34	5	8	6
Ni	108	86	104	93	8	5	6	9	3	2	3	4	2	3	1	4	2
Cu	32	25	35	43	16	15	12	18	5	3	4	11	14	13	2	3	2
V	684	607	570	441	270	249	274	236	38	47	23	93	75	41	90	71	30
Zn	104	112	102	123	76	63	58	81	95	86	79	51	48	63	12	17	13
Zr	215	134	225	185	113	157	106	85	56	74	110	34	29	43	105	75	94
CIPW Norm																	
Q	8.02	9.27	10.36	0.22	14.17	21.06	18.16	9.93	32.21	33.33	29.89	27.38	24.35	28.98	35.45	37.7	37.46
Or	4.51	2.99	1.97	2.76	7.79	11.67	20.04	6.83	8.83	6.53	9.14	10.74	7.22	5.67	4.03	11.38	8.1
Ab	18.09	16.66	15.93	19.71	39.94	23.94	10.43	20.32	11.82	22.74	18.78	9.61	15.08	17.02	38.32	30.36	29.85
An	18.65	19.09	18.86	23.5	6.15	13.47	16.15	22.24	18.75	12.74	21.77	20.73	25.48	24.48	3.33	6.69	10.31
C	0	0	0	0	0	0.05	0	0	0	0	0	0	0.58	0.96	0	0	1.68
Di	11.84	10.05	9.33	13.39	1.34	0	27.71	6.57	11.62	4.93	2.53	10.52	0	0	1.3	6.75	1.4
Hy	13.88	17.77	20.55	24.78	14.25	17.08	0.05	20.86	5.21	7.16	8.62	7.06	13.86	10.33	7.01	2.39	7.1
Mt	21.04	20.71	19.88	14.74	13.46	11.13	4.69	11.58	9.86	10.95	8.68	11.89	12.67	12.1	10.16	4.01	4.54
Il	2.15	1.8	1.53	0.71	0.92	0.76	0.88	1.46	0.59	0.74	0.37	0.18	0.36	0.36	0.2	0.09	0.74
Ap	1.82	1.64	1.6	0.2	2.01	0.83	1.88	0.21	1.11	0.89	0.21	1.89	0.41	0.1	0.21	0.62	0.21

6.2. MNF transformation. The minimum noise fraction (MNF) transformation is used to determine the inherent dimensionality of image data, to segregate noise in the data, and to reduce the computational requirements for subsequent processing [37]. The MNF transform as modified from

Green *et al.* [38] is essentially two cascaded Principal Component transformations. The first transformation, based on an estimated noise covariance matrix, decorrelates and rescales the noise in the data. This first step results in transformed data in which the noise has unit variance and no

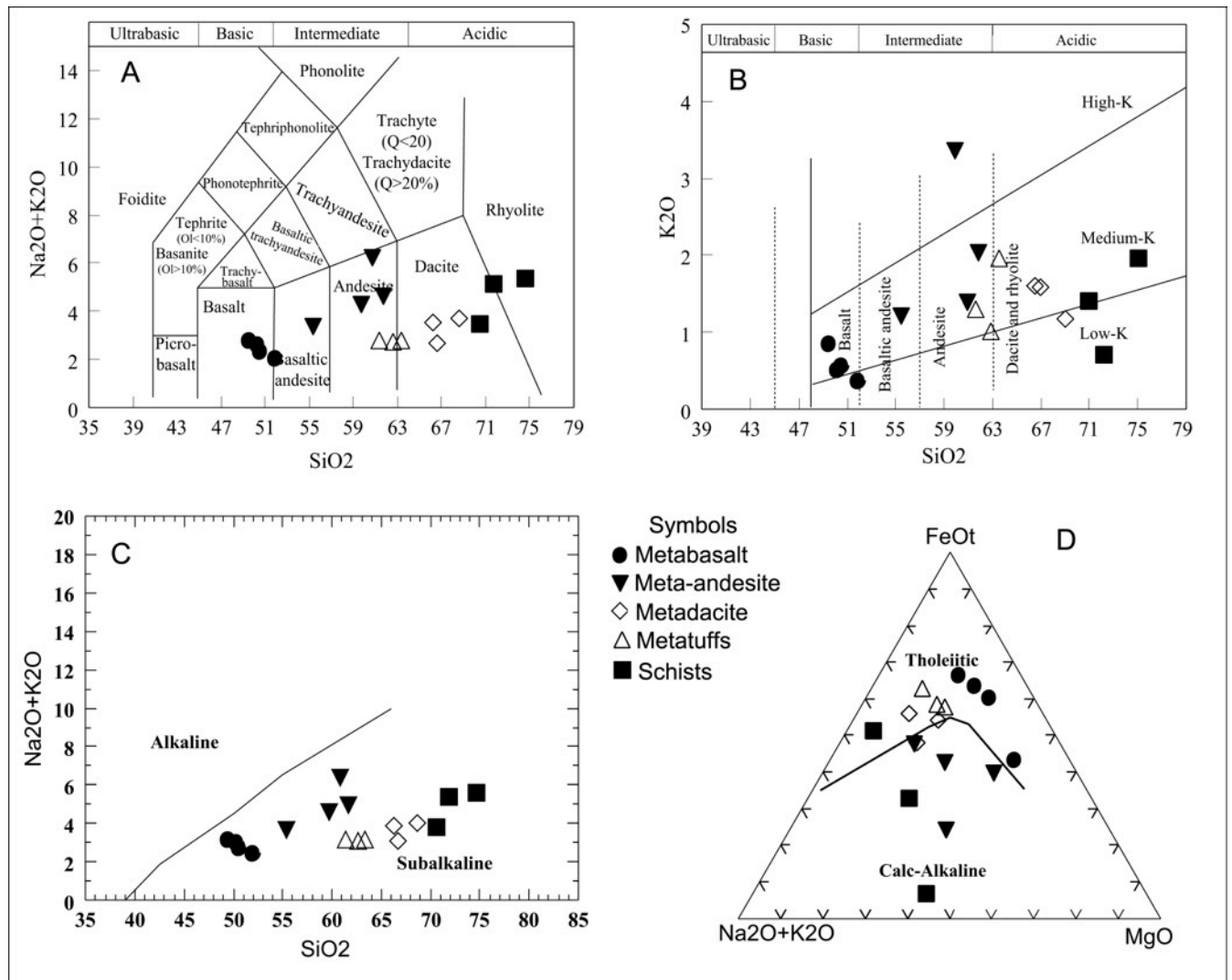


Fig. (5). Plots of the analyzed metavolcanics and metavolcanosediments on **A)** the (K_2O+Na_2O) versus SiO_2 and **B)** the K_2O versus SiO_2 diagrams [23], as well as on **C)** the (K_2O+Na_2O) versus SiO_2 and **D)** the AFM diagrams [24].

band-to-band correlations. The second step is a standard Principal Components transformation of the noise-whitened data. The MNF transformation technique was applied on the non-thermal six ETM+ bands. Single band black-and-white MNF-images as well as false color composite MNF-images were generated. The MNF-transformation showed that the altered rocks are easily identified using the black-and-white MNF-4 image (Fig. 9A) where they show distinct white image signature. The processed false color composite MNF-image was generated from combination of MNF4, MNF3 and MNF2 in red, green and blue respectively (Fig. 9B). The image easily identifies the alteration zones that have reddish and rose image signatures. The meta-andesite shows purple image signature, whereas the metavolcanosediments have light pink and green image signatures. Moreover, this FCC MNF-image failed to differentiate between metabasalt, metadacite and quartz diorite that exhibit similar light blue image signatures.

6.3. Band Ratio Technique. Band rationing is an extremely useful processing technique for enhancing features in geologic remote sensing, e.g. [39-48]. Drury [49] prepared simply the band ratio by dividing the digital number (DN)

values of each pixel in one band by the corresponding DN values of another band. Since ratios seldom fall outside the range 0.25 - 4.0, in order to display the ratio the values must be re-scaled to 0-255 range. Band ratio technique enhances the objects based on the differences in reflectivity between the numerator and denominator spectral bands. The 5/7, 4/5 and 3/1 band ratio images of study area were generated to recognize and differentiate between the different varieties of metavolcanics and metavolcanosediments. On the 5/7 band ratio image (Fig. 10A) the talc-carbonates and serpentinites appear with bright image signature, whereas the metabasalt, metadacite and quartz-diorite show dark image signature. The meta-andesite and metavolcanosediments show gray image signature. On the 4/5 band ratio image (Fig. 10B) schists have bright image signature whereas talc carbonate rocks have dark image signature. Sabins [36] stated that the spectra of iron minerals (goethite, hematite and jarosite) show low blue reflectance and high red reflectance. Nearly all rock units exposed in the study area have gray image signature on 3/1 band ratio image and this means that different concentrations of iron minerals occur within these rock units.

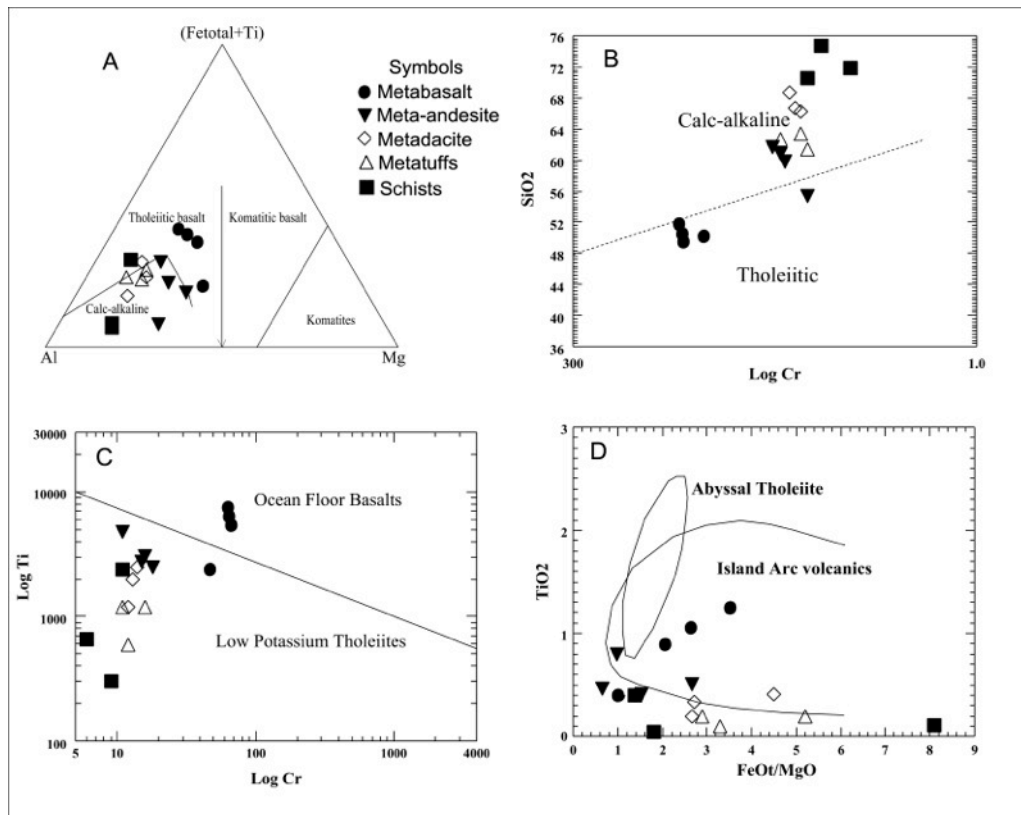


Fig. (6). Plots of the analyzed metavolcanics and metavolcanosediments on **A)** the Al-(Fe^{total}+Ti)-Mg diagram [25], **B)** the Log Cr - SiO₂ diagram [26], **C)** the Log Cr-Log Ti diagram [27] and **D)** the TiO₂ - FeO*/MgO diagram [28].

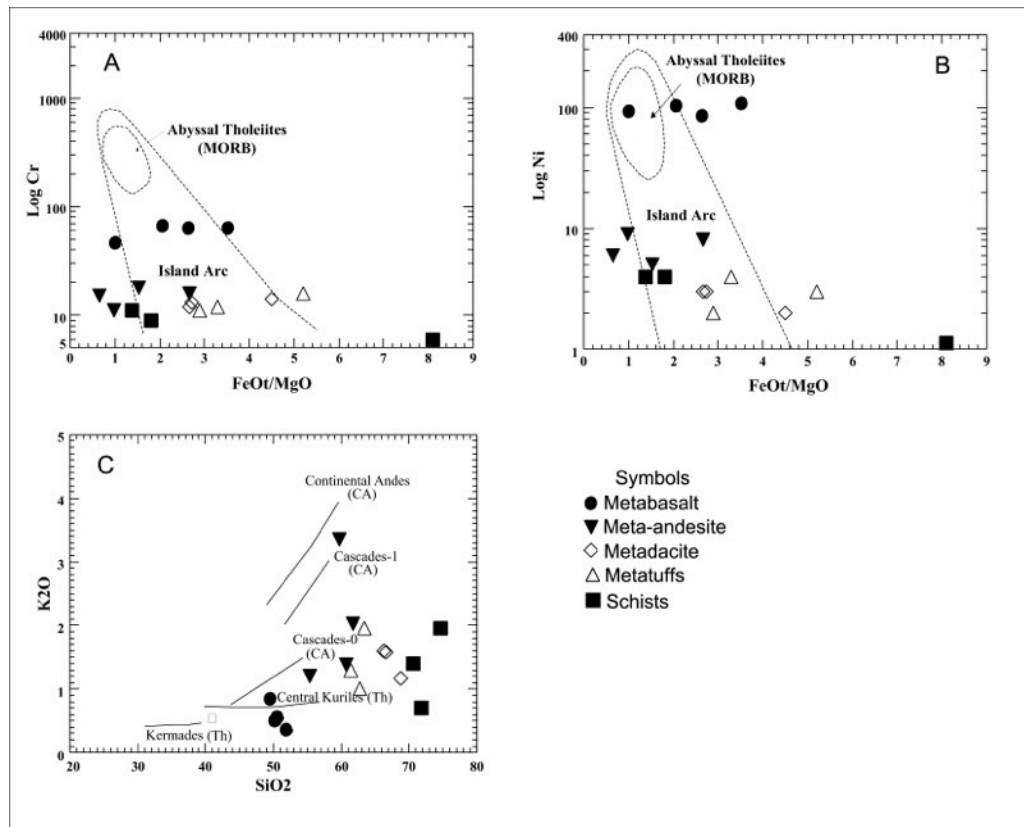


Fig. (7). Plots of the analyzed metavolcanics and metavolcanosediments on **A)** the Log Cr versus FeO*/MgO [26], **B)** the Log Ni versus FeO*/MgO [29] and **C)** the K₂O versus SiO₂ diagram [30].

Table 2. Eigen-Values and Variances % of the Landsat-7 Subset of Marahiq

Eigen Channel	Eigen-Values	Var. %
PC1	1344.16	93.50
PC2	74.12	5.16
PC3	9.67	0.67
PC4	5.29	0.37
PC5	2.98	0.21
PC6	1.38	0.09

The information extracted from the three band ratio images was integrated into one false color composite image (5/7:R, 4/5:G & 3/1:B) as shown in (Fig. 11A). The serpentinite and talc carbonate rocks have red and rose image signatures respectively, whereas the metabasalt and meta-andesite have green and dark red image signatures, respectively. This processed FCC ratio image failed to discriminate clearly between basic and acidic rocks. For examples, the metabasalt, metadacite and quartz-diorite have nearly the same green image signature. Accordingly, another FCC ratio image should be integrated to discriminate between these units. The FCC ratio image (5/7:R, 5/1:G & 5/4*3/4:B) was processed to differentiate between acidic and

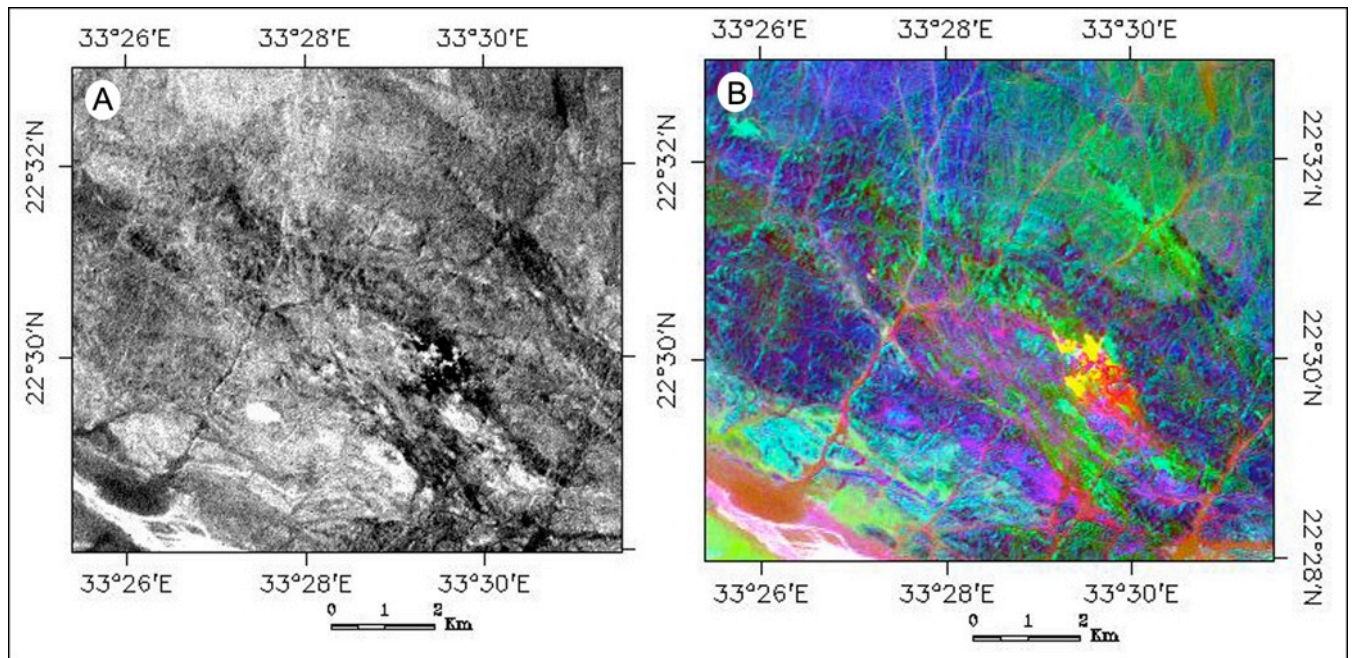


Fig. (8). A) PC4 image showing altered rocks with white tone, B) FCC PC image (PC1:R, PC2:G, PC4:B).

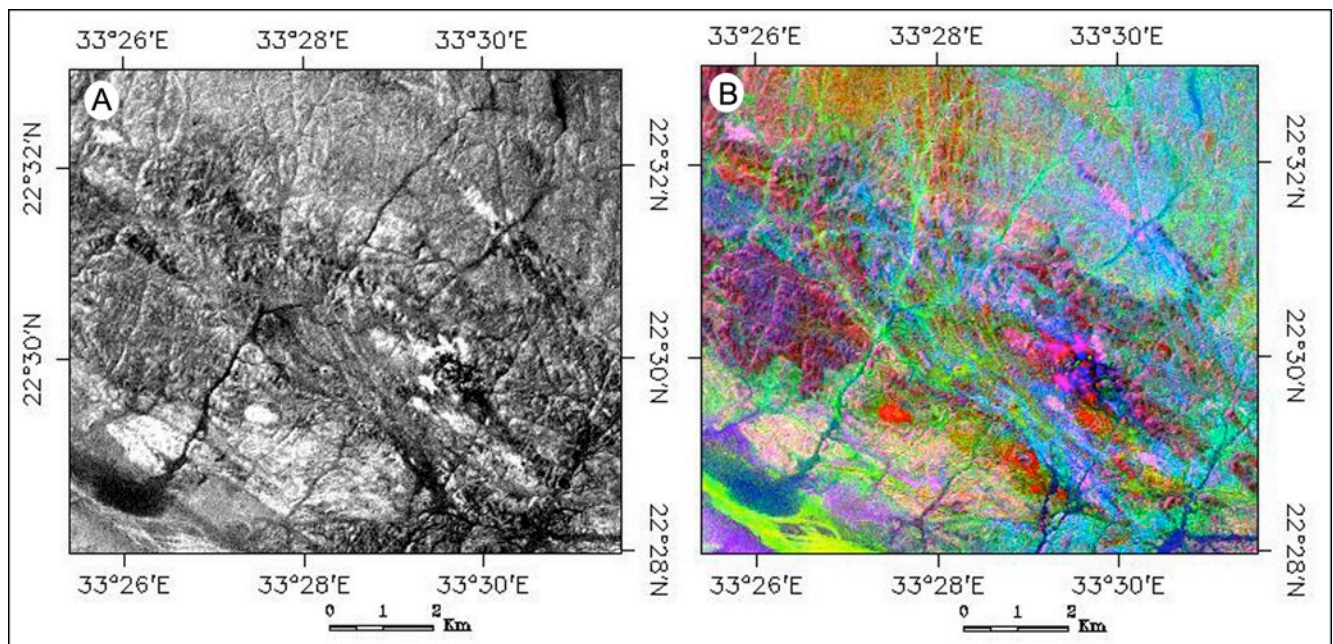


Fig. (9). A) MNF4 image showing altered rocks with white tone, B) FCC MNF image (MNF4:R, MNF3:G, MNF2:B).

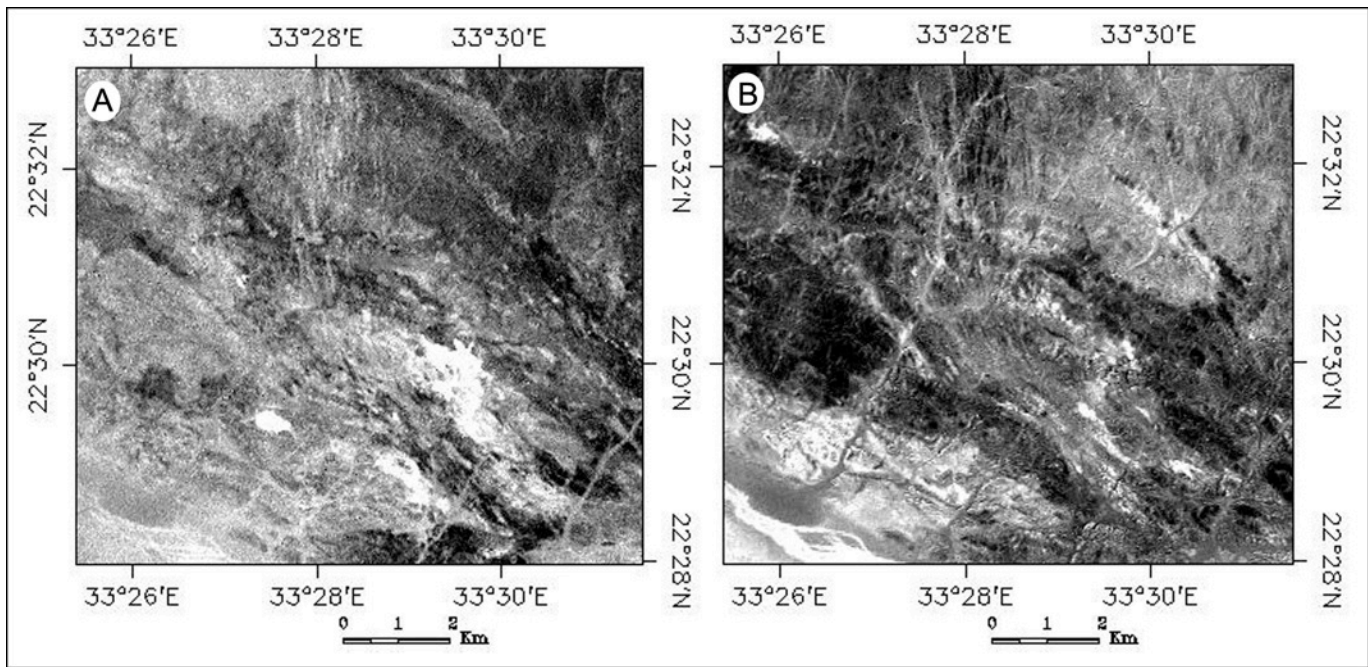


Fig. (10). A) 5/7 band ratio image and B) 4/5 band ratio image.

basic rock units (Fig. 11B). The basic and acidic rock units have dark blue and dark green image signatures respectively. Integration of all information extracted from the processed ETM+ images resulted in generation of a new detailed geologic map for the study area (Fig. 12).

7. CONCLUSIONS

The island arc metavolcanics and metavolcano-sediments of the Marahiq area are differentiated in to metabasalt, meta-andesite, metadacite and meta-andesitic tuffs, while the metavolcanosediments are chlorite-talc schist and biotite-chlorite schist. Geochemically, the investigated

metavolcanics and metavolcanosediments rocks are calc-alkaline to tholeiite in nature with low to medium-K content. These rocks were developed within an island arc tectonic setting. The gray-scale PC4, MNF4 and 5/7 ratio images are best delineating the altered rocks within shear zones. The information extracted from processed gray-scale and FCC images led to generation of a new detailed map of the Marahiq area.

CONFLICT OF INTEREST

The authors declare that there are no conflicts of interest.

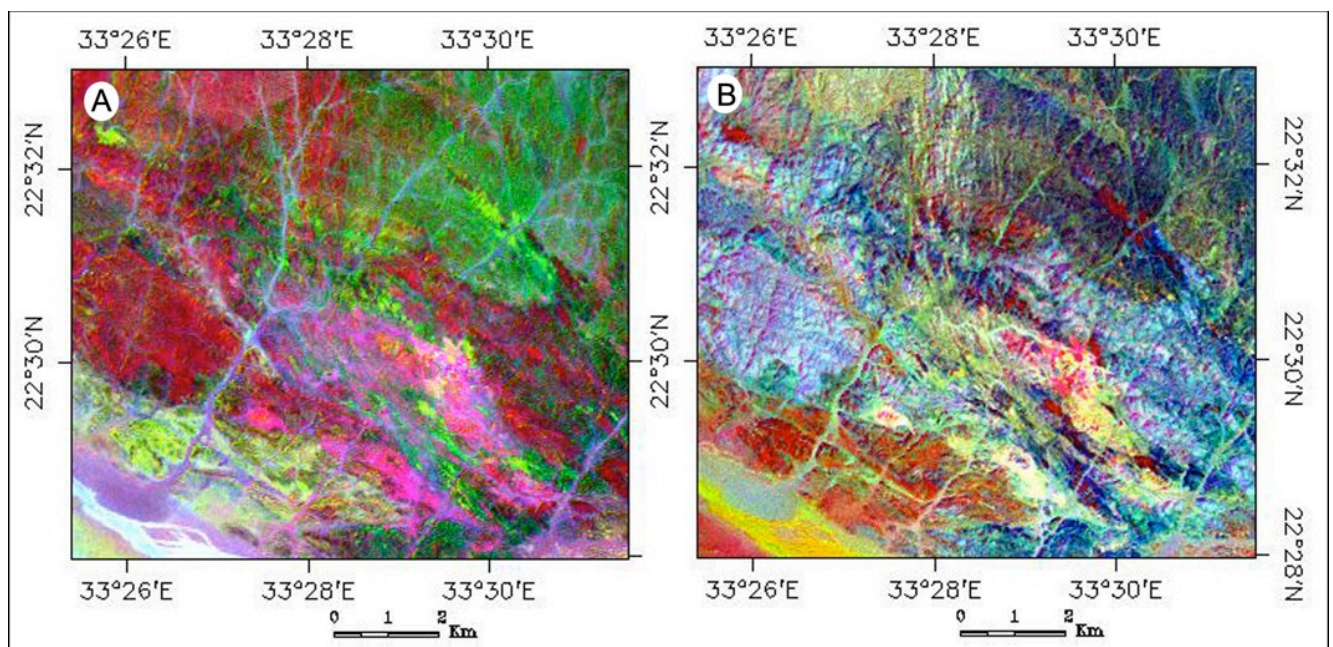


Fig. (11). A) FCC ratio image (5/7:R, 4/5:G, 3/1:B) and B) FCC ratio image (5/7:R, 5/1:G, 5/4*3/4:B).

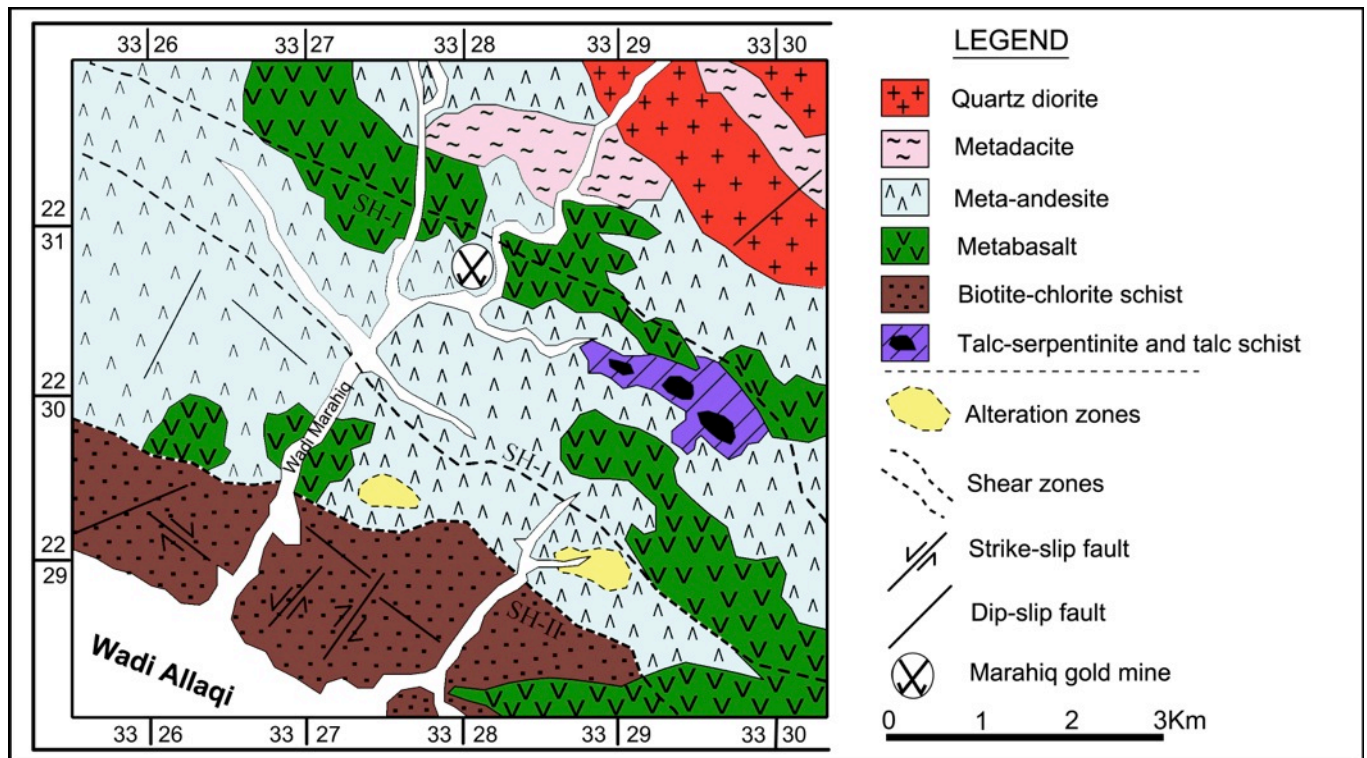


Fig. (12). Detailed geologic map, generated by using the processed remote sensing images, shows distribution of island arc assemblage rocks at Marahiq area.

ACKNOWLEDGEMENTS

The authors are grateful to Prof. Dr. M. M. Hassaan, Professor of Economic Geology and Geochemistry, Al-Azhar University for supervising all the steps of the study and critical reading of the manuscript.

REFERENCES

- [1] Kroner A, Todt W, Hussein IM, Mansour M, Rashwan AA. Dating of late Proterozoic ophiolites in Egypt and the Sudan using the single grain zircon evaporation technique. *Precambrian Res* 1992; 59: 15-32.
- [2] Shackleton RM. Review of late Proterozoic sutures, ophiolitic melanges and tectonics of eastern Egypt and north-east Sudan. *Geologische Rundschau* 1994; 83: 537-46.
- [3] Shackleton RM, Ries AC, Graham RH, Fitches WR. Late Precambrian Ophiolitic mélange in the Eastern Desert of Egypt. *Nature* 1980; 285: 472-4.
- [4] Gass IG. Upper Proterozoic (Pan-African) calc-alkaline magmatism in Northeastern Africa and Arabia. In Thorpe RS, Ed. *Andesites and Related Rocks*. New York: John Wiley & Sons 1982; pp. 591-609.
- [5] Bentor YK. The crustal evolution of the Arabo-Nubian massif with special reference to the Sinai Peninsula. *Precambrian Res* 1985; 28: 1-74.
- [6] Stern RJ, Hedge CE. Geochronologic and isotopic constraints on late Precambrian crustal evolution in the Eastern desert of Egypt. *Am J Sci* 1985; 285: 97-127.
- [7] Kroner A, Greiling R, Reischmann T, *et al*. Pan-African crustal evolution in the Nubian segment of north-east Africa. *Am Geophys Union Spec Publ* 1987; 17: 235-57.
- [8] El Gaby S, List FX, Tehrani R. Geology, evolution and metallogenesis of the Pan-African Belt in Egypt. In: El Gaby S, Greiling RO, Eds. *The Pan African Belt of Northeast Africa and adjacent areas. Tectonic Evolution and Economic Aspects of a Late Proterozoic Orogen*. Earth Evolution Sciences. Frieder Vieweg and Sohn, Braunschweig/Wiesbaden 1988; pp. 17-68.
- [9] Stern RJ, Sellers G, Gottfried D. Bimodal dyke swarms in the North Eastern Desert of Egypt: significance for the origin of late Precambrian "A-type" granites in northern Afro-Arabia. In: El Gaby S, Greiling RO, Eds. *The Pan-African Belt of Northeast Africa and Adjacent Areas*. Vieweg: Weisbaden 1988; pp. 147-77.
- [10] Hassan MA, Hashad AH. Precambrian of Egypt. In: Said R, Ed. *The geology of Egypt*. Balkama: Rotterdam 1990; pp. 201-45.
- [11] Kroner A, Eyal M, Eyal Y. Early Pan-African evolution of the basement around Elat, Israel, and the Sinai Peninsula revealed by single-zircon evaporation dating, and implications for crustal accretion rates. *Geology* 1990; 18: 545-8.
- [12] El Gaby S. Geologic and tectonic framework of the Pan-African orogenic belt in Egypt. 2nd Int Conf Geology of the Arab World, Cairo University 1994; pp. 3-17.
- [13] Stern RJ. Arc assembly and continental collision in the Neoproterozoic East African Orogen: implications for the consolidation of Gondwana land. *Ann Rev Earth Planetary Sci* 1994; 22: 319-51.
- [14] Abdel Khalek ML, Takla MA, Sehim A, Abdel Wahed M, Hamimi Z, Sakran ShM. Tectonic evolution of the Shield rocks, east Wadi Beitan area, southeastern Desert, Egypt. *Egypt J Geol* 1999; 43(1): 1-25.
- [15] Abdel Salam MG, Stern RJ. Sutures and shear zones in the Arabian-Nubian shield. *J Afr Earth Sci* 1996; 23: 289-310.
- [16] Ghoneim MF, Lebda ME. Metavolcanic and older granites of the central Eastern Desert of Egypt are cogenetic island arc regime: Mineralogical and geochemical evidences. 3rd Conf Geochem 1997; 153-70.
- [17] El Kazzaz YA. Speculations on the tectonic Evolution of Central Wadi Allaqi, South Eastern Desert, Egypt. *Proceedings of the Egyptian Geol Surv, Centennial Confer (1896-1996) Cairo, 19-22 Nov 1996*; pp. 205-23.
- [18] El Kazzaz, YA, Taylor WEG. A tectonic-stratigraphy of Neoproterozoic in Wadi Allaqi, South Eastern Desert, Egypt. *Proceedings of the Egyptian Geol. Surv., Centennial Confer (1896-1996), Cairo, 19-22 Nov., 225-262*.
- [19] Emam A. Ore-microscopy, geochemistry of host rocks, and concentration patterns of gold and associated elements, Marahiq gold mine, South Eastern Desert, Egypt. MSc Thesis, Geol Depart, Aswan Fac of Sci South Valley University 1999; p. 301.

- [20] Berhe SM. Ophiolites in northeast and east Africa: implications for Proterozoic crustal growth. *J Geol Soc Lond* 1990; 147: 41-57.
- [21] Taylor WE, El-Kazzaz YA, Rashwan AA. An outline of the tectonic framework for the Pan-African orogeny in the vicinity of Wadi Um Relan area, South Eastern Desert, Egypt. In: Thorweihe U, Schandelmeier H, Eds. *Geoscientific Research in Northeast Africa* 1993; pp. 31-4.
- [22] Greiling RO, Abdeen MM, Dardir AA, *et al.* A structural synthesis of the Proterozoic Arabian-Nubian Shield in Egypt. *Geol Rundsch* 1994; 83: 484-501.
- [23] Le Maitre RW, Bateman P, Dudek A, *et al.* A classification of igneous rocks and glossary of terms. Blackwell: Oxford 1989; p. 193.
- [24] Irvine TN, Baragar WRA. A guide to the chemical classification of the common volcanic rocks. *Can J Earth Sci* 1971; 8: 523-48.
- [25] Jensen LS. A New Cation Plot for Classifying Subalkalic Volcanic Rocks: Ontario Division of Mines MP 66 1976; 22.
- [26] Miyashiro A, Shido F. Tholeiitic and calc-alkaline series in relation to the behaviours of titanium, vanadium, chromium and nickel. *Am J Sci* 1975; 275: 265-77.
- [27] Pearce JA. Basalt geochemistry used to investigate post-tectonic environments on Cyprus. *Tectonophysics* 1975; 25: 41-67.
- [28] Miyashiro A. Volcanic rock series and tectonic setting. *Annu Rev Earth Planet Sci* 1975a; 3: 251-69.
- [29] Miyashiro A. Classification, characteristics and origin of ophiolites *J Geol* 1975b; 83: 249-81.
- [30] Miyashiro A. Volcanic rock series in island arcs and active continental margins. *Am J Sci* 1974; 274: 321-55.
- [31] Drury SA. *Image Interpretation in Geology*. 1st ed. Allen & Unwin (Publishers) Ltd: London 1987; p. 43.
- [32] Sabins FF. *Remote Sensing Principles and Interpretation*. 2nd ed. San Francisco Freeman 1987; p. 449.
- [33] Gupta AP. *Remote sensing geology*. Berlin-Heidelberg: Springer 1991; p. 356.
- [34] Moik H. *Digital processing of remotely sensed images: NASA SP no. 431*, Washington, D.C 1980.
- [35] Singh A, Harrison A. Standardized principal components. *Int J Remote Sens Lond* 1985; 6(6): 883-96.
- [36] Sabins, FF Jr. *Remote Sensing: Principles and Interpretation*. 3rd ed. New York: Freeman 1997; p. 494.
- [37] Boardman JW, Kruse FA. Automated spectral analysis: A geologic example using AVIRIS data, north Grapevine Mountains, Nevada. In proceedings, Tenth Thematic Conference on Geologic Remote Sensing, Environmental Research Institute of Michigan Ann Arbor 1994; MI: 407-18.
- [38] Green AA, Berman M, Switzer P, Craig MD. A transformation for ordering multispectral data in terms of image quality with implications for noise removal. *IEEE Trans Geosci Remote Sens* 1988; 26(1): 65-74.
- [39] Sultan M, Arvidson RE, Sturchio NC. Mapping of serpentinites in the Eastern Desert of Egypt using Landsat Thematic Mapper data. *Geology* 1986; 14: 995-9.
- [40] Sultan M, Arvidson RE, Sturchio NC, Guinness EA. Lithologic mapping in arid regions with Landsat TM data: Meatiq dome, Egypt. *Geol Soc Am Bull* 1987; 99: 748-62.
- [41] Rothery DA. Improved discrimination of rock units using Landsat Thematic mapper imagery of the Oman Ophiolite. *J Geol Soc Lond* 1987; 144: 587-97.
- [42] Frei M, Jutz SL. Use of Thematic Mapper data for the detection of gold bearing formations in the eastern Desert of Egypt. In: *Proceedings of the 7th Thematic Conference on Remote Sensing for Ore Exploration Geology* 1989; II: 1157-72.
- [43] Sabins FF. Remote sensing for mineral exploration. *Ore Geol Rev* 1999; 14: 157-83.
- [44] Madani AA, Abdel Rahman E, Fawzy KhM, Emam AA. Mapping of the hydrothermal alteration zones at Haimur gold mine area, South Eastern Desert, Egypt, using remote sensing techniques. *Egypt. J Remote Sens Space Sci* 2003; 6: 47-60.
- [45] Gad SA, Kusky TM. Lithological mapping in the Eastern Desert of Egypt, the Barramiya area, using Landsat thematic mapper (TM). *J Afr Earth Sci* 2006; 44: 196-202.
- [46] Gad S, Kusky T. ASTER spectral ratioing for lithological mapping in the Arabian-Nubian Shield, the Neoproterozoic Wadi Kid area, Sinai, Egypt. *Gondwana Res* 2007; 11: 326-35.
- [47] Madani A, Emam A. SWIR ASTER band ratios for lithological mapping and mineral exploration: a case study from El Hudi area, South Eastern Desert, Egypt. *Arab J Geosci* 2011; 4(1): 45-52.
- [48] Zoheir B, Emam A. Integrated analysis of field, mineralogical and satellite imagery data for geologic mapping and exploration targets in the greenstone terrane of South Eastern Desert, Egypt. *J Afr Earth Sci* 2012; 66-67: 22-34.
- [49] Drury SA. *Image Interpretation in Geology*. 2nd ed, Chapman and Hall: London 1993; p. 283.

Received: April 2, 2013

Revised: November 18, 2013

Accepted: February 2, 2014

© Emam *et al.*; Licensee Bentham Open.This is an open access article licensed under the terms of the Creative Commons Attribution Non-Commercial License (<http://creativecommons.org/licenses/by-nc/3.0/>) which permits unrestricted, non-commercial use, distribution and reproduction in any medium, provided the work is properly cited.